Journal of Catalysis 285 (2012) 292–303

Contents lists available at SciVerse ScienceDirect

Journal of Catalysis

journal homepage: www.elsevier.com/locate/jcat

Nb effect in the nickel oxide-catalyzed low-temperature oxidative dehydrogenation of ethane

Haibo Zhu [a], Samy Ould-Chikh [a], Dalaver H. Anjum [b], Miao Sun [a], Gregory Biausque [a], Jean-Marie Basset [a], Valérie Caps [a,*]

[a] *KAUST Catalysis Center, 4700 King Abdullah University of Science and Technology, Thuwal 23955-6900, Saudi Arabia*
[b] *FEI Company, 5350 NE Dawson Creek Drive, Hillsboro, OR 97124, USA*

ARTICLE INFO

Article history:
Received 24 May 2011
Revised 4 October 2011
Accepted 8 October 2011
Available online 12 November 2011

Keywords:
Nickel
Niobium
Nanocomposites
Oxidative dehydrogenation
Ethane

ABSTRACT

A method for the preparation of NiO and Nb–NiO nanocomposites is developed, based on the slow oxidation of a nickel-rich Nb–Ni gel obtained in citric acid. The resulting materials have higher surface areas than those obtained by the classical evaporation method from nickel nitrate and ammonium niobium oxalate. These consist in NiO nanocrystallites (7–13 nm) associated, at Nb contents >3 at.%., with an amorphous thin layer (1–2 nm) of a niobium-rich mixed oxide with a structure similar to that of $NiNb_2O_6$. Unlike bulk nickel oxides, the activity of these nanooxides for low-temperature ethane oxidative dehydrogenation (ODH) has been related to their redox properties. In addition to limiting the size of NiO crystallites, the presence of the Nb-rich phase also inhibits NiO reducibility. At Nb content >5 at.%, Nb–NiO composites are thus less active for ethane ODH but more selective, indicating that the Nb-rich phase probably covers part of the unselective, non-stoichiometric, active oxygen species of NiO. This geometric effect is supported by high-resolution transmission electron microscopy observations. The close interaction between NiO and the thin Nb-rich mixed oxide layer, combined with possible restructuration of the nanocomposite under ODH conditions, leads to significant catalyst deactivation at high Nb loadings. Hence, the most efficient ODH catalysts obtained by this method are those containing 3–4 at.% Nb, which combine high activity, selectivity, and stability. The impact of the preparation method on the structural and catalytic properties of Nb–NiO nanocomposites suggests that further improvement in NiO-catalyzed ethane ODH can be expected upon optimization of the catalyst.

1. Introduction

Ethylene is a major raw material of the petrochemical industry. It is indeed used in the production of commodity chemicals, such as ethylene oxide and polyethylene. It is currently produced together with propylene by high temperature steam cracking of naphtha [1]. This thermal process, involves gas phase free-radical chemistry; it results in a mixture of various types of hydrocarbons [2], with low yields of ethylene. These yields can be improved by cracking LPG (Liquefied Petroleum Gas) [3]. Energy input and carbon emissions can be lowered, to a certain extent, by catalytic approaches, which at the same time allow tuning the ethylene to propylene ratio [4]. However, these highly endothermic processes suffer from high energy demand and complex thermal management [5].

These limitations could be waived by producing ethylene under oxidizing conditions, from catalytic oxidative dehydrogenation (ODH) of ethane. Many materials have been shown to catalyze this reaction, such as rare-earth oxides [6–9], alkaline/alkaline-earth metals [10–12], perovskites [13–18], and transition metal oxides [19–23]. Among this latter class, mixed oxides selectively produce ethene at particularly low temperature. It is the case of Mo^{V}-based systems [24] (doped with Nb) initially developed in 1978 by Thorsteinson et al. [25] and refined later by Lopez Nieto et al. [26] and, more recently, NiNbTa-based systems discovered by a combinatorial approach in 2003 [27]. This last discovery followed the observation that nickel oxides displayed high activity and selectivity for low-temperature ethane ODH [28]. This was somehow unexpected due to the high activation energy of oxygen desorption from NiO [29]. The efficiency of nickel oxides catalysts was initially improved by using them unsupported, instead of supporting them onto inorganic materials [30,31]. Later, another strategy was to dope NiO with various elements such as Li, Mg, Al, Ga, Ti, Nb, Ta [32], and very recently W [33]. Among these elements, niobium turned out to be the best [34]. These dopants influence not only the amount but also the mobility of oxygen species present in the catalytic oxides. According to Lemonidou et al., niobium reduces the number of active sites for oxygen dissociation by filling the cationic vacancies. This would enhance the diffusion

---

* Corresponding author.
E-mail address: valerie.caps@kaust.edu.sa (V. Caps).

0021-9517/$ - see front matter © 2011 Elsevier Inc. All rights reserved.
doi:10.1016/j.jcat.2011.10.005

of unselective, “electrophilic” O^- oxygen species inside the bulk and increase the number of less labile, selective, “nucleophilic” O^{2-} oxygen species on the catalyst surface [35]. However, it was recently suggested that the occurrence of structural doping was limited to a few percent of Nb and that the superiority of the $Ni_{0.85}Nb_{0.15}O_{1.225}$ catalyst (lower intrinsic activity but higher selectivity) was due to the presence of an amorphous Nb-rich oxide phase (Nb_2O_5, $NiNb_2O_6$) covering part of NiO crystallites surface and thus part of the active, non-selective sites [36].

In this context, we present an alternative method for the synthesis of Ni and Ni–Nb catalysts. This sol–gel-based method, starting from nickel nitrate, niobium chloride, and citric acid, produces oxides with high surface areas. It leads to highly active and stable nickel oxides. The optimum levels of Nb doping is reduced, and results in both high efficiency (conversion $*$ selectivity) and high stability in low-temperature ethane ODH.

2. Experimental

2.1. Catalyst preparation

$NiCl_2$ (98%, Aldrich), $Ni(NO_3)_2$. $6H_2O$ (98.5%, Aldrich), $NbCl_5$ (99%, Strem), Niobium oxalate hydrate ($C_{10}H_5NbO_{20}{\cdot}xH_2O$, Alfa Aesar), oxalic acid (99%, Aldrich), citric acid (99.5%, Aldrich), ammonia (28% in H_2O, Aldrich) were commercially available and used without further purification.

2.1.1. Preparation of nickel oxides

Protocol 1: precipitation by reaction between nickel nitrate and oxalic acid. 1.81 g of oxalic acid was dissolved in 100 mL of ethanol, and this solution was added dropwise into a solution containing 5.75 g $Ni(NO_3)_2$ and 100 mL ethanol. The obtained blue precipitates were separated by filtration and then washed with ethanol and water several cycles. The last blue solid was dried at 100 °C for 12 h and subsequently calcined at 400 °C for 4 h. It is referred to as $NiO_{\text{–oxalic acid}}$.

Protocol 2: precipitation by reaction between nickel chloride and ammonia. 3 mL $NH_3{\cdot}H_2O$ (28 vol.%) was dissolved in 100 mL H_2O to get diluted ammonia solution, which was added to a $NiCl_2$ solution (4.69 g in 200 mL H_2O) slowly (approximately 3 h) under vigorous stirring (300 rpm) at room temperature. The resulting precipitates were filtered and washed with distilled water several times. After drying at 90 °C for 12 h, the precipitates were heated at 400 °C for 4 h. It is referred to as $NiO_{\text{–NH4OH}}$.

Protocol 3: sol–gel by reaction between nickel nitrate and citric acid. The sol–gel method was inspired from [37]. 3 g of $Ni(NO_3)_2{\cdot}6H_2O$ and 6 g of citric acid were dissolved in 50 mL of H_2O. The blue solution was aged at 80 °C under stirring for 24 h and then evaporated at 80 °C in an open system to eliminate water. The obtained gel was further dried at 120 °C and 140 °C, respectively, for 2 h and lastly dried at 160 °C for 12 h. The resulting black xerogel was calcined by heating from room temperature to 450 °C with a rate of 1 °C/min and then kept at this temperature for 4 h in static air. It is referred to as $NiO_{\text{–SG}}$. After calcination at 450 °C, a shiny layer of metal-like material appeared on the surface of the black NiO powder. That metallic micro-sheet was easily removed using a spatula, without contaminating the powder, referred to as $NiO_{\text{–SG}}$ (Ni removed).

2.1.2. Preparation of Nb_2O_5

Nb_2O_5 was prepared by calcination of Niobium oxalate hydrate at 450 °C (ramp rate of 1 °C/min from room temperature to 450 °C) for 4 h in static air.

2.1.3. Preparation of Nb-doped NiO

*Protocol 3**. $Ni_xNb_{1-x}O$ (x = 0.99, 0.98, 0.97, 0.96, 0.95, 0.90, 0.85, 0.80), which will be referred to as Nb_{1-x}–Ni_xO in the following, were prepared by modifying the sol–gel protocol for nickel oxide (Protocol 3) as follows for the, e.g., $Nb_{0.15}$–$Ni_{0.85}O$ composition. 0.46 g $NbCl_5$ was slowly added to 30 ml H_2O. The resulting white $Nb_2O_5{\cdot}nH_2O$ precipitate was washed with H_2O until free of chlorine. It was then dissolved in warm citric acid solution (50 mL, 0.63 mol L^{-1}). When 3 g of $Ni(NO_3)_2{\cdot}6H_2O$ were added, the initially transparent solution turned blue. It was kept at 80 °C in a closed system for 24 h and then under stirring for 12 h to remove the water. The gel was dried in 3 steps. First, it stayed at 120 °C for 2 h. Second, it was then heated to 140 °C and kept at this temperature for 2 h. Third, the gel was dried at 160 °C for 12 h. The obtained black xerogel was calcined at 450 °C (ramp rate of 1 °C/min from room temperature to 450 °C) for 4 h in static air.

2.2. Catalyst characterization

Thermogravimetric analyses (TGA) in air were performed on a Mettler–Toledo. The uncalcined samples were heated from 50 to 800 °C with a rate of 10 °C/min in a flow of air (100 mL/min).

N_2 adsorption/desorption isotherms were acquired on a Micromeritics ASAP2420. The samples were degassed for 2 h at 300 °C before nitrogen adsorption. Surface areas of the samples were analyzed by multipoint BET analysis method, and pore volumes were estimated at $P/P_0 = 0.99$.

The morphologies of the catalyst were imaged with an FEI Quanta 600 FEG environmental scanning electron microscope (ESEM). The catalyst was sputter-coated with gold in argon atmosphere before measurement to make it conductive.

X-ray photoelectron spectroscopy (XPS) was carried out on a Kratos AXIS Ultra DLD spectrometer, using a monochromatic Al Kα X-ray source operating at 45 W and a pass energy of 20 eV. The binding energies of Nb 3d core levels are referenced to the C 1s core level at 285.0 eV.

Temperature-programmed reduction (TPR) was performed on an Altamira Instrument equipped with a TCD detector; data were analyzed using the AMI analysis Software. The catalyst powder (25 mg) was placed in a U-shaped quartz reactor and pretreated in flowing Ar (30 mL/min) for 0.5 h at 350 °C, followed by cooling to room temperature. The temperature was then raised from room temperature to 800 °C at a rate of 10 °C/min with a 5% H_2/Ar flow (30 mL/min). The uptake of the H_2 was estimated by 5 blank pulse calibrations.

Rietveld X-ray diffraction intensity data sets were collected using a Bruker D8 Advanced A25 diffractometer in Bragg–Brentano geometry fitted with a copper tube operating at 40 kV and 40 mA and a linear position sensitive detector (opening 2.9°). The diffractometer was configured with a 0.18° diverging slit, 3.2° anti scattering slit, 2.5° Soller slits, and a Ni filter. The data sets were acquired in continuous scanning mode (0.007182°/s) over the 2θ range 10–140°, using a step interval of 0.05° and a counting time of 7 s per step.

The XRD data were analyzed by the Rietveld method using the fundamental-parameters (FPs) approach contained within the software TOPAS V4.2 (Bruker-AXS) [38]. For consistency, the same refinement procedure was used for all samples. *Bunsenite* and metallic nickel reflections were both refined with a cubic structure (space group F_{m-3m} (no. 225)) with initial cell parameters of 4.18 and 3.52 Å, respectively. The profile parameters included the scale factor, a sample displacement parameter, and a five-term polynomial for the background (zero to fourth order coefficients). The FPs approach calculates analytically the instrumental resolution function. Crystallite size then becomes a function of the Lorentzian peak broadening. Refined structural parameters are the site occupation factor of nickel and the isotropic atomic displacement parameter of nickel and oxygen. Strong correlation between atomic displacement parameters and site occupation factor prevented the structure refinement to be conclusive about the occurrence of bulk niobium doping.

Additional peaks localized at 2θ = 30.43, 35.64, 41.22, 43.80, and 60.82°, characteristic of $NiNb_2O_6$ [ICSD card: 37212] [36,39], were fitted with a pseudo-Voigt function and used to improve the overall quality of the refinement. Indeed, the latter peaks are in vicinity of *bunsenite* reflections and tend to influence the calculation of *bunsenite* crystallite size when not taken into account. Those reflections are considered as an amorphous Ni_xNb_yO phase which might constitute a precrystalline network of the crystalline mixed oxide $NiNb_2O_6$, that was identified by HRTEM-FFT studies described below. Evolution of the amorphous content as a function of Nb content was roughly computed by calculating a pseudo degree of crystallinity ρ.

$$\rho = \frac{\text{Total peak areas of crystalline phases}}{\text{Total peak areas of crystalline phases} + \text{Total peak areas of NixNbyO amorphous phase}}$$

R_{wp}, R_{Bragg}, GOF were, respectively, in the range of 0.9, 0.7, and 1.8 for all refinements.

Imaging of samples was performed on a Titan G^2 80–300 kV transmission electron microscope (TEM) from FEI Company (FEI Company, Hillsboro, OR) equipped with a 4 k × 4 k changed couple device (CCD) camera model US4000 and an energy filter model GIF Tridiem from Gatan, Inc. (Gatan Inc., Pleasanton, CA). Multiple locations of the specimens are investigated using high-resolution transmission electron microscopy (HRTEM) technique. The acquired HRTEM micrographs were processed to obtain their diffractograms using Fast-Fourier transforms (FFT) technique to measure the spatial frequencies present in the images. The measurement of the spatial frequencies allowed obtaining the d-spacings of the phases present in the sample with an error less than 5%. The TEM was also set to scanning TEM (STEM) mode for carrying out the electron energy loss spectroscopy (EELS) characterization of sample with about ~1 nm spatial resolution. Energy resolution of GIF in EELS mode was nearly 1 eV, and furthermore, it was set to an energy dispersion of 0.2 eV/channel. EELS signal from Oxygen K edge (O-K edge) of 532 eV is acquired with convergence angle of 9 mrad and collection angle of ~20 mrad. GIF was also utilized in energy-filtered TEM (EFTEM) mode for the distribution of Ni- and Nb-based phases in the samples. Ni M-edge of energy 68 eV and Nb M-edge of energy 205 eV were selected for their EFTEM maps. Furthermore, each elemental map is created by using a 3-window method of generating such maps in GIF.

3. Catalyst evaluation in low-temperature ethane oxidative dehydrogenation (ODH)

Catalytic properties are evaluated at atmospheric pressure in the oxidative dehydrogenation of ethane using a P and ID micropilot equipped with a stainless steel reactor (internal diameter 4 mm). Gas mixtures of 10% C_2H_6/5% O_2 and 10% C_2H_6/10% O_2 in He are introduced through the catalytic bed at a total flow rate of 10 mL/min. Gas compositions are controlled by calibrated mass-flow controllers. 100 mg catalyst was placed in the reactor with glass wool as support (W/F = 0.6 g s/mL). It is ramped at 1°/min from 200 to 400 °C. The reaction mixture is sampled at the outlet of the reactor at regular intervals, typically every 5 min, and analyzed with on-line Varian 490 micro-GC equipped with a TCD detector and two columns: a MolSieve 5 Å column (Ar as carrier gas) to quantify O_2 (no CO is detected under our conditions), and a poraPLOT Q column (He as carrier gas) to quantify CO_2, C_2H_4 as well as C_2H_6. Ethane conversion and selectivity to ethylene are calculated on a carbon basis. To obtain different conversion levels at constant temperature (330 °C), the W/F ratio is varied from 0.05 to 0.6 g s/mL. For stability tests, gas mixtures of 10% C_2H_6/5% O_2 in He are introduced through the catalytic bed held at 330 °C, at a total flow rate of 10 mL/min (W/F = 0.6 g s/mL), and the reaction mixture is sampled every 30 min for about 70 h.

4. Results and discussion

4.1. NiO catalysts

4.1.1. Morphology

Three methods were considered for the preparation of NiO catalysts: precipitation of nickel nitrate in oxalic acid (Protocol 1), precipitation of nickel chloride in ammonia (Protocol 2) and a sol–gel method starting from nickel nitrate and citric acid (Protocol 3). The specific surface areas and porosities, as well as the corresponding scanning electron micrographs, are given in Table 1 and Fig. 1.

The morphologies of the materials prepared by precipitation are consistent with the morphology obtained in [37] by precipitation of nickel nitrate in ammonia, with similar scanning electron micrographs (Fig. 1) and surface areas of 60–65 m^2/g (Table 1). The nickel oxide prepared by sol–gel exhibits a lower surface area of 31 m^2/g. It is attributed to the presence of the more dense Ni metallic phase (14 wt.% present in $NiO_{\_SG}$, as determined by XRD, Table 2), which appeared after calcination at 450 °C in the form of a shiny black micro-sheet on top of the black NiO powder. The use of citric acid in the synthesis, which remains in the dry gel as evidenced by TGA, indeed results in incomplete oxidation of NiO after calcination at 450 °C, as observed in [40]. After removal of the shiny nickel micro-sheet (<1 wt.% Ni left in $NiO_{\_SG}$ (Ni removed)), the surface area reaches a value of 48 m^2/g. This is lower than the 88 m^2/g obtained in [37], despite the fact that the NiO crystallite size (13 nm, Table 2) is similar (10 nm). It is also lower than the theoretical surface (69 m^2/g) expected for spheres of NiO (density 6.67 g/cm^3) of 13 nm in diameter. This indicates a certain degree of aggregation of the NiO crystallites, in agreement with SEM observations (Fig. 1).

4.1.2. Catalytic properties in ethane ODH

These nickel oxides prepared by three different methods have been tested in low-temperature ODH of ethane (Fig. 2). Despite lower surface area (48 m^2/g) and presence of <1 wt.% Ni metal, $NiO_{\_SG}$ exhibits a higher efficiency than $NiO_{\_NH4OH}$, which is similar to that displayed by $NiO_{\_oxalic\ acid}$. The intrinsic activity of $NiO_{\_SG}$, in terms of number of mole of ethane converted per surface unit per time unit (Table 3, Entry 3), is similar to that reported for nickel oxides prepared by the evaporation method [34,36]. But, given the high selectivity of our catalyst (Table 3, Entry 3), the efficiency of $NiO_{\_SG}$ is 2–3 times higher than those reported so far, with a surface-specific ethene production rate at 350 °C of 3.9×10^{-8} $mol_{ethene}/m^2/s$. Finally, given the low surface area of the published nickel oxides (17 m^2/g [34] and 12 m^2/g [36]), the mass-specific ethene production rate (Table 3, Entry 3) is one order of magnitude higher on our 48 m^2/g $NiO_{\_SG}$ and ethene yields of 9% and 24% are obtained at 300 °C and 350 °C, respectively (Table 3, Entry 3).

These preliminary results clearly show the impact of the preparation method on the structural and catalytic properties of nickel oxides catalysts for low-temperature ethane ODH. The selectivity of about 60% displayed by $NiO_{\_SG}$ (held up to 25% conversion) is significantly higher than selectivities normally reported for pure nickel oxides (20% [34] – 30% [36]). It is normally only achieved with composite materials, such as the recently reported nickel oxide supported on high surface area zirconia, which managed to

Table 1
Physico-chemical properties of nickel oxides prepared by three different methods of preparation.

Catalyst	Method of preparation	Surface area (m^2/g)	Average pore size (nm) on ads	Mesopore volume (10^{-3} cm^3/g)
$NiO_{-oxalic\ acid}$	Precipitation ($Ni(NO_3)_2$/oxalic acid)	65	8.0	153
NiO_{-NH4OH}	Precipitation ($NiCl_2$/ammonia)	60	18	267
NiO_{-SG} (including Ni)	Sol–gel ($Ni(NO_3)_2$/citric acid)	31	9.2	85
NiO_{-SG} (Ni removed)	Sol–gel ($Ni(NO_3)_2$/citric acid)	48	5.7	82

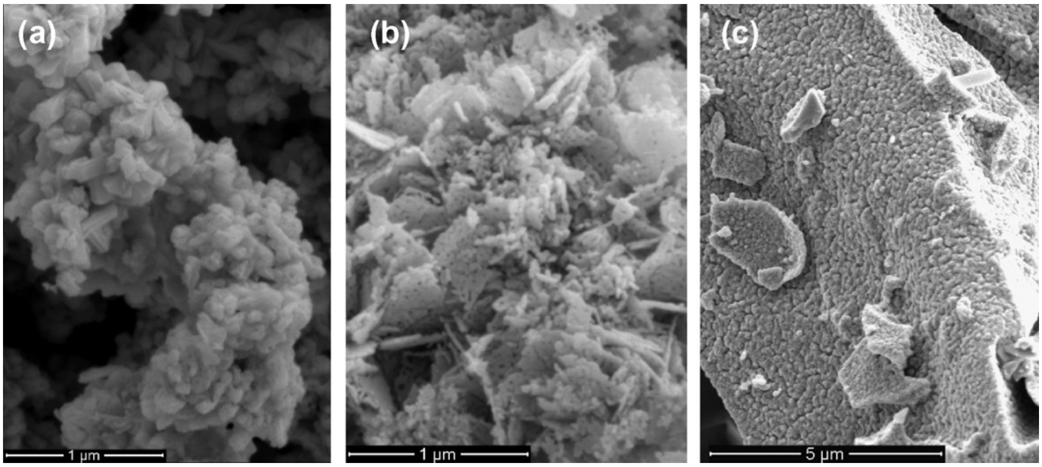

Fig. 1. SEM micrographs of nickel oxides prepared by Protocol 1 (a), Protocol 2 (b), and Protocol 3 (c).

Table 2
Structural properties of nickel-based oxides based on Rietveld analysis of the diffractograms.

Catalyst	Crystalline composition (wt.%)		Crystallinity degree (%)	Crystallite size (nm)		Cell parameter[a] (Å)	
	NiO	Ni		NiO	Ni	NiO	Ni
$NiO_{-oxalic\ acid}$	100	0	100	13	–	4.180	–
NiO_{-NH4OH}	100	0	100	12	–	4.182	–
NiO_{-SG} (including Ni)	86	14	100	13	102	4.179	3.525
NiO_{-SG} (Ni removed)	99	1	100	13	102	4.179	3.525
$Nb_{0.01}$–$Ni_{0.99}O$	81	19	96	13	38	4.179	3.525
$Nb_{0.02}$–$Ni_{0.98}O$	100	<1	95	10	–	4.180	3.525
$Nb_{0.03}$–$Ni_{0.97}O$	100	0	93	7	–	4.184	–
$Nb_{0.04}$–$Ni_{0.96}O$	100	<1	89	7	–	4.184	3.525
$Nb_{0.05}$–$Ni_{0.95}O$	100	0	92	9	–	4.180	–
$Nb_{0.10}$–$Ni_{0.90}O$	100	0	84	9	–	4.179	–
$Nb_{0.15}$–$Ni_{0.85}O$	100	0	66	10	–	4.180	–
$Nb_{0.20}$–$Ni_{0.80}O$	100	0	69	10	–	4.178	–

[a] Cell parameters are given with a typical mean square deviation of 0.001 Å.

reach a selectivity to ethene of 55% (at 24.8% conversion obtained at 450 °C with ethane/O_2 = 2) [41]. Hence, by combining high activity and an exceptionally high selectivity for pure NiO, undoped nickel oxides prepared in the presence of citric acid can be remarkably efficient catalysts for low-temperature ethane ODH.

4.2. Nb_{1-x}–Ni_xO catalysts ($0.80 \leqslant x \leqslant 0.95$)

4.2.1. Morphology

By incorporating Niobium in the sol–gel method at similar loading (5–20 at.%) as those published (see Experimental Part), the surface areas of the resulting materials increase significantly. The material containing only 5 at.% Nb readily displays a surface area of 130 m^2/g (Table 4), which increases with increasing Nb loading until it reaches a maximum at 225 m^2/g for $Nb_{0.15}$–$Ni_{0.85}O$. This is, to the best of our knowledge, the highest surface area ever reported for such oxides. The diffraction patterns are slightly broadened and can be fitted with the *bunsenite* NiO phase with a lattice parameter of 4.179 ± 0.001 Å and a crystallite size of about 9–10 nm (Table 2), regardless of the Nb loading.

The measured surface areas are thus higher than the calculated surface of NiO spheres of 9–10 nm in diameter (90–100 m^2/g). This cannot be accounted for by the doping of the nickel oxide cubic structure with Nb atoms. First, the expected contraction of the NiO lattice [34] is not observed (Table 2). Second, given the molecular weights of Ni (58.7 g/mol) and of Nb (92.9 g/mol), replacing one Ni^{2+}–Ni^{3+} pair with one Nb^{5+} (which creates one nickel vacancy) would result, at the maximum doping of 20 at.%, in a ca. 4% decrease in the weight of a given crystallite. The change in the volume of the crystallite being negligible, such a 20 at.% doping of NiO crystals would thus result in a maximum of 4% increase in the surface area of the crystal. Besides, filling cationic vacancies with Nb^{5+} cations (which, for each vacancy filled, causes reduction of five Ni^{3+} into five Ni^{2+}) would result in an increase in the weight of the crystal and thus a decrease in its surface area.

The significant increase in surface areas can be explained, on the other hand, by the presence of a less dense, amorphous Ni_xNb_yO

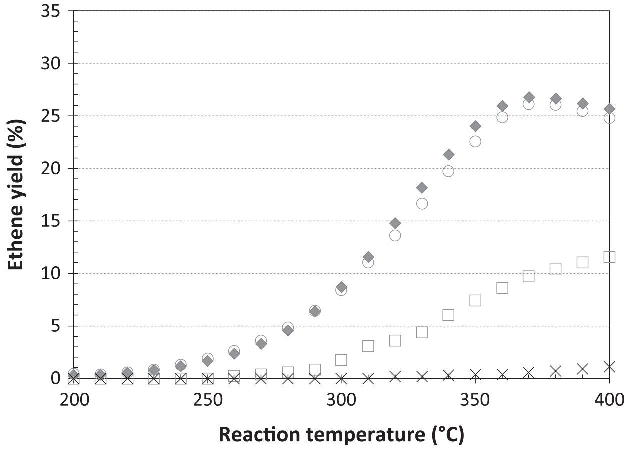

Fig. 2. Ethene yield as a function of temperature, obtained in ethane ODH over NiO$_{\text{–oxalic acid}}$ (○), NiO$_{\text{–NH4OH}}$ (□), NiO$_{\text{–SG}}$ (◆) and Nb_2O_5 (×). Reaction conditions: 10% C_2H_6/10% O_2/80% He, W/F = 0.6 g s/mL.

phase, with a concentration that increases with increasing Niobium content. Bright field images (Fig. 3a) obtained by high-resolution transmission electron microscopy performed on $Nb_{0.20}$–$Ni_{0.80}O$ indeed show areas containing essentially amorphous particles. These particles contain an intimate mixture of nickel and niobium, as indicated by EFTEM (Fig. 3b). The Nb/Ni ratio is not only superior to the theoretical 1/4 ratio, but also much larger than 1 (EELS). The diffractograms from the couple of Nb-rich areas shown in Fig. 3a clearly indicate that some parts are completely amorphous (Fig. 3c), while other parts display the possible crystalline signature of $NiNb_2O_6$ (d_{002} = 2.51 Å and d_{312} = 2.05 Å, Fig. 3d). The presence of this latter phase was also identified in Ni–Nb–O samples prepared by the evaporation method [36,39]. Including a broad contribution of this phase (2θ = 30.43, 35.64, 41.22, 43.80, and 60.82° [ICSD: 37212]) in the Rietveld analysis of the diffractograms allowed us to significantly improve the refinement. According to the evolution of the crystallinity degree, it can represent a non-negligible part of the sample (Table 2).

Besides, Table 2 shows that the Ni phase is absent from the diffractograms of all these Nb-containing samples. Formation of metallic Ni upon calcination at 450 °C of the Nb–Ni–citrate gel is thus prevented. This can be due to the higher M/citric acid ratio (M = Nb + Ni), when increasing the amount of $NbCl_5$ in the synthetic mixture. It is consistent with the higher amount of residue retained after complete decomposition of the citrate component upon TGA in air (at about 450 °C): 30 wt.% for $Nb_{0.20}$–$Ni_{0.80}O$ instead of 21 wt.% for NiO$_{\text{–SG}}$ (Table 4). It also suggests that the presence of Nb in the Ni–citrate gel hinders the reduction of Ni by citrate. This can possibly be due to a kind of geometric effect: the Nb atoms located near the nickel atoms would increase the distance between the citrate component and the nickel atoms and thus act as a kind of barrier. The absence of any citrate residue after calcination at 450 °C (absence of $\nu_{\text{C–H}}$ and $\nu_{\text{C=O}}$ vibrations in FTIR spectra) excludes the formation/occurrence of high surface area hybrid NiO–citrate networks [42]. Alternatively, it strongly indicates that the high surface areas observed indeed stem from the presence of very small nanoobjects of niobium-rich oxide, of about 1.6 nm for $Nb_{0.15}$–$Ni_{0.85}O$, for example, considering non-aggregated 10 nm NiO crystallites and a density of 5.644 g/cm^3 for $NiNb_2O_6$. A brief XPS study of Nb 3d core levels in $Nb_{0.15}$–$Ni_{0.85}O$ shows a binding energy for Nb 3d$_{5/2}$ of 207.0 eV. It is shifted by −0.4 eV, as compared with Nb^{V} in Nb_2O_5 (207.4 eV [43]), and by +0.2 eV, as compared with Nb^{V} in $NaNbO_3$ (206.8 eV [44]). This is consistent with a close interaction between Nb and Ni, which electronegativity is lower than that of O and higher than that of Na on the Pauling scale. This further supports the presence of an amorphous mixed Ni–Nb oxide phase, such as $NiNb_2O_6$.

4.2.2. Catalytic properties in ethane ODH

With these systems, the ethene yields systematically decrease with increasing Nb content (Fig. 4). This decrease occurs despite the higher surface area of the Nb-containing samples (130–225 m^2/g), as compared with that of NiO$_{\text{–SG}}$ (48 m^2/g). The low ethene yields result from a much lower intrinsic activity of the Nb-containing nickel oxides (from 4.2×10^{-9} mol$_{\text{ethane converted}}$/m^2/s to 1.8×10^{-8} mol$_{\text{ethane converted}}$/m^2/s at 350 °C), as compared with that of NiO$_{\text{–SG}}$, which is not compensated by the otherwise significantly higher selectivity of the Nb-containing catalysts (Table 3). These results could be explained by the presence of a Nb-based thin layer on the NiO crystallite surface, which prevents access to part of O$^-$ active species, as proposed by Millet et al. [36]. This is supported by EFTEM micrographs from areas containing numerous NiO crystallites (Fig. 5a and b): NiO nanocrystals indeed appear covered and surrounded by an amorphous niobium-rich phase (Fig. 5c).

4.3. Nb_{1-x}–Ni_xO catalysts ($0.96 \leqslant x \leqslant 0.99$)

4.3.1. Morphology

At lower Nb contents (<4 at.%), the overall morphology of the Nb–Ni oxides (Fig. 6) consists in 20–30-nm particles with a spherical

Table 3
Catalytic properties of nickel-based oxides in low-temperature ethane ODH (Reaction conditions: 10% C_2H_6/10% O_2/80% He, W/F = 0.6 g s/mL, temperature ramped at 1°/min from 200 to 400 °C).

Catalyst	Ethane conversion (%)		Selectivity (%)		Ethene yield (%)		Ethane ODH rate (mol/m^2/s)		Ethene production rate (mol/g/s)		Ea[a] (kJ/mol)		
	300 °C	350 °C	300 °C	350 °C	300 °C	350 °C	300 °C ($\times 10^{-8}$)	350 °C ($\times 10^{-8}$)	300 °C ($\times 10^{-7}$)	350 °C ($\times 10^{-6}$)	ODH	Ethene	CO_2
NiO$_{\text{–oxalic acid}}$	15	43	55	53	8.4	23	1.76	4.9	6.3	1.7	79	77	78
NiO$_{\text{–NH4OH}}$	16	35	8	21	1.3	7.4	1.97	4.3	0.9	0.6	100	114	96
NiO$_{\text{–SG}}$	15	42	59	57	8.7	24	2.40	6.8	6.5	1.8	80	80	80
$Nb_{0.01}$–$Ni_{0.99}O$	11	32	63	60	6.7	19	1.43	4.3	5.0	1.4	79	78	80
$Nb_{0.02}$–$Ni_{0.98}O$	13	36	65	62	8.3	23	1.05	3.0	6.2	1.7	78	77	79
$Nb_{0.03}$–$Ni_{0.97}O$	16	41	64	62	9.9	25	1.05	2.8	7.4	1.9	79	78	80
$Nb_{0.04}$–$Ni_{0.96}O$	13	39	68	64	9.2	25	0.69	2.0	6.8	1.9	80	79	82
$Nb_{0.05}$–$Ni_{0.95}O$	10	31	74	68	7.6	21	0.59	1.8	5.7	1.6	77	75	82
$Nb_{0.10}$–$Ni_{0.90}O$	9	27	78	70	7.0	19	0.42	1.3	5.2	1.4	77	77	81
$Nb_{0.15}$–$Ni_{0.85}O$	6	19	83	76	5.2	14	0.21	0.6	3.9	1.1	77	75	86
$Nb_{0.20}$–$Ni_{0.80}O$	3	10	81	75	2.5	8	0.13	0.4	1.9	0.6	77	75	85

[a] Calculated by the Arrhenius law, on the variations of the mass-specific rates of ethane consumption and net ethene and CO_2 production (mol/g/s) as a function of the temperature (K^{-1}), in the 210–310 °C temperature range.

Table 4
Physico-chemical properties of nickel-based oxides prepared by sol–gel method (Protocol 3*).

Catalyst	Surface area (m^2/g)	Average pore size (nm) on ads	Mesopore volume (10^{-3} cm^3/g)	Residue amount (wt.%) (TGA–air)
$NiO_{\_SG}$	48	5.7	82	21
$Nb_{0.05}$–$Ni_{0.95}O$	130	5.1	158	22
$Nb_{0.10}$–$Ni_{0.90}O$	160	4.5	148	25
$Nb_{0.15}$–$Ni_{0.85}O$	225	3.3	128	25
$Nb_{0.20}$–$Ni_{0.80}O$	185	3.9	124	30

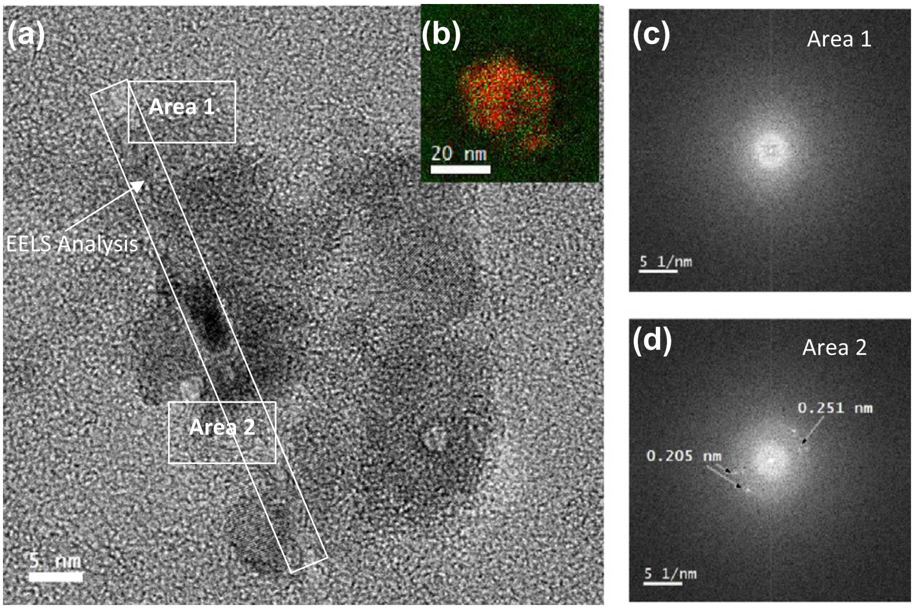

Fig. 3. (a) Bright field HRTEM image of an area in $Nb_{0.20}$–$Ni_{0.80}O$ containing amorphous Ni_xNb_yO. (b) EFTEM of the same area, niobium appears in green and nickel in red. (c) Local FFT of Area 1: this area contain only amorphous phase. (d) Local FFT of Area 2 presenting two characteristics d-spacings of $NiNb_2O_6$. (For interpretation of the references to color in this figure legend, the reader is referred to the web version of this article.)

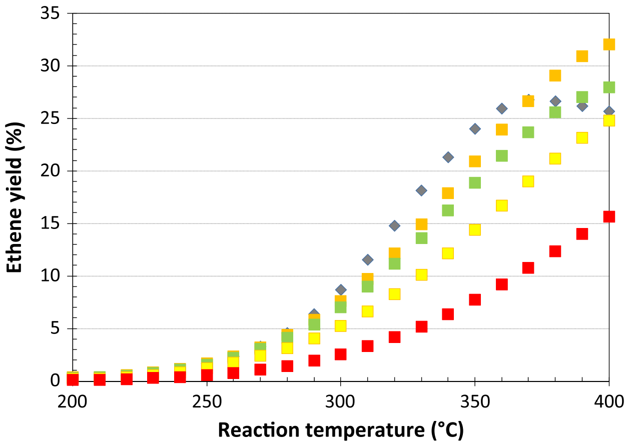

Fig. 4. Ethene yield as a function of temperature, obtained by ethane ODH (10 vol.% O_2) over nickel oxide-based catalysts issued from Protocol 3*: $NiO_{\_SG}$ (◆), $Nb_{0.05}$–$Ni_{0.95}O$ (🟧), $Nb_{0.10}$–$Ni_{0.90}O$ (🟩), $Nb_{0.15}$–$Ni_{0.85}O$ (🟨) and $Nb_{0.20}$–$Ni_{0.80}O$ (🟥). Reaction conditions: 10% C_2H_6/10% O_2/80% He, W/F = 0.6 g s/mL.

shape, which are similar to those displayed by $NiO_{\_SG}$ and highly loaded Nb_{1-x}–Ni_xO. The diffraction pattern of $Nb_{0.01}$–$Ni_{0.99}O$ is similar to that of Nb-free $NiO_{\_SG}$ (before removal of Ni), with an average NiO crystallite size of about 13 nm and the presence of 18 wt.% Ni metallic phase (Table 2). On the other hand, the diffraction patterns of $Nb_{0.02}$–$Ni_{0.98}O$, $Nb_{0.03}$–$Ni_{0.97}O$, and $Nb_{0.04}$–$Ni_{0.96}O$ are more similar to those displayed by the Nb-rich NiO samples. First, the Ni metallic phase is absent from the diffractograms. This indicates that a loading of 2 at.% Nb in the Nb–Ni–citrate gel is enough to disturb reduction to Ni by citrate upon calcination. Second, the NiO crystallite sizes of 10 nm in $Nb_{0.02}$–$Ni_{0.98}O$ and 7 nm in $Nb_{0.03}$–$Ni_{0.97}O$ and $Nb_{0.04}$–$Ni_{0.96}O$ are lower than those observed in $NiO_{\_SG}$ and $Nb_{0.01}$–$Ni_{0.99}O$ samples (13 nm) and close to those displayed by Nb-rich samples (9–10 nm). Finally, all samples contain a significant amount of an amorphous phase (Table 2), which is present as a broad contribution in the diffraction patterns. The surface areas (Table 5) are consistent with samples containing aggregated 7–13 nm NiO crystallites and a small amount of extra-crystalline, amorphous, nanometric Nb-rich mixed oxides. At the 4at% Nb content in particular, the surface area exceeds the external surface displayed by unaggregated 7 nm NiO crystallites (129 m^2/g). A potential effect of Nb on lowering the degree of aggregation of NiO crystallites is thus not enough to explain the high value observed (145 m^2/g). This latter effect can however not be excluded.

4.3.2. Catalytic properties in ethane ODH

Ethene yields obtained over these materials are very similar to those obtained on 48 m^2/g $NiO_{\_SG}$ (Fig. 7a). The two formulations containing the smallest NiO crystallites (7 nm) and the largest lattice parameter (4.184 Å), $Nb_{0.03}$–$Ni_{0.97}O$ and $Nb_{0.04}$–$Ni_{0.96}O$, however, seem slightly more efficient. This is confirmed by decreasing the amount of oxygen in the reactant feed, i.e., by performing ethane ODH in the presence of 5 vol.% instead of 10 vol.% O_2 (Fig. 7b). The high yields, of up to 10% at 300 °C and 25% at 350 °C in the presence of 10 vol.%O_2, come from slightly lower intrinsic activities (between 2.0×10^{-8} $mol_{ethane\ converted}/m^2/s$ and 2.8×10^{-8} $mol_{ethane\ converted}/m^2/s$ at 350 °C) associated with higher

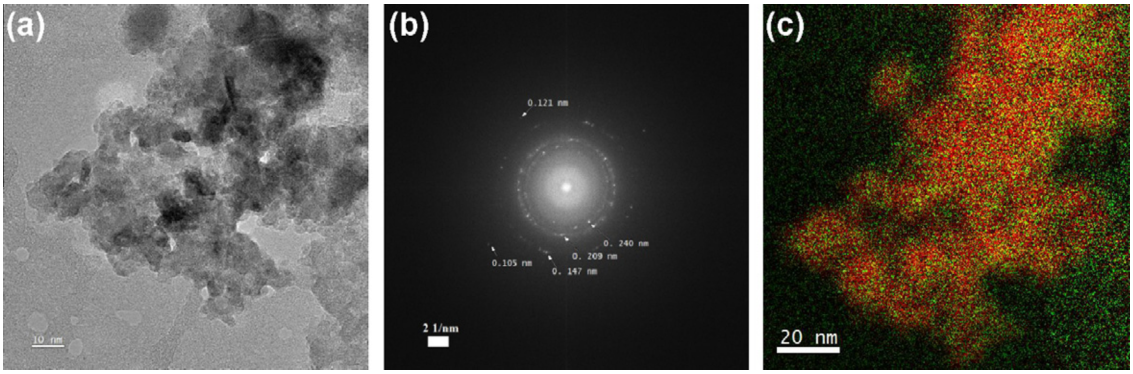

Fig. 5. (a) Bright field HRTEM image of an area containing numerous crystalline NiO particles in $Nb_{0.20}–Ni_{0.80}O$, (b) FFT of same area presenting characteristic d-spacings of the *bunsenite* structure, and (c) color map generated from Ni and Nb EFTEM maps of the same area, niobium appears in green and nickel in red. (For interpretation of the references to color in this figure legend, the reader is referred to the web version of this article.)

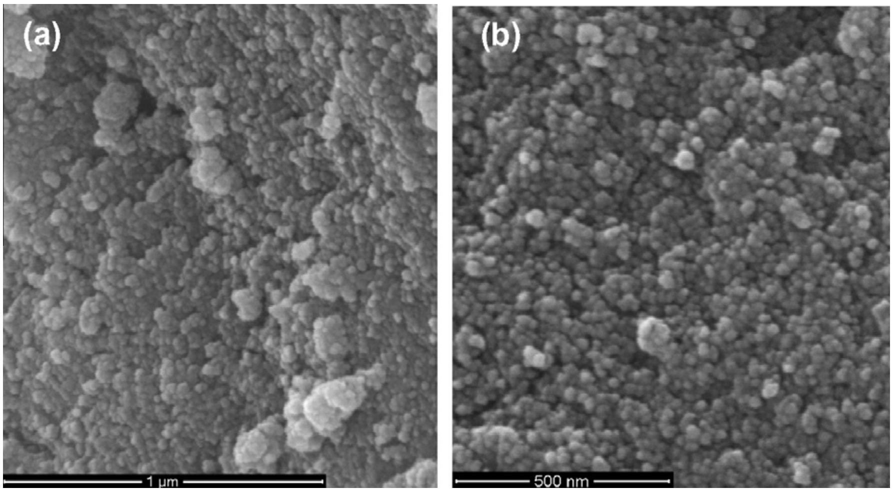

Fig. 6. SEM micrographs of low-loaded Nb-containing nickel oxides prepared by Protocol 3*: $Nb_{0.03}–Ni_{0.97}O$ (a) and $Nb_{0.02}–Ni_{0.98}O$ (b).

Table 5
Physico-chemical properties of nickel-based oxides prepared by sol–gel method (Protocol 3*).

Catalyst	Surface area (m^2/g)	Average pore size (nm) on ads	Mesopore volume (10^{-3} cm^3/g)	Residue amount (wt.%) (TGA–air)
$NiO_{\_SG}$	48	5.7	82	21
$Nb_{0.01}–Ni_{0.99}O$	56	6.2	90	29
$Nb_{0.02}–Ni_{0.98}O$	90	5.9	145	30
$Nb_{0.03}–Ni_{0.97}O$	110	3.8	90	33
$Nb_{0.04}–Ni_{0.96}O$	145	3.3	92	30

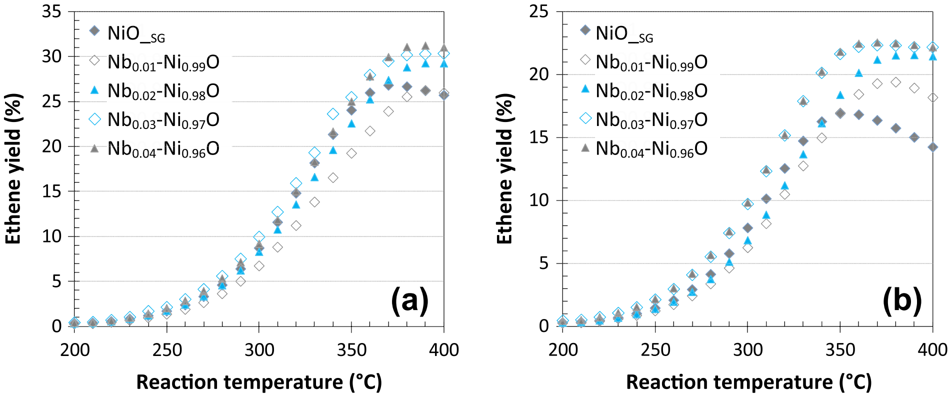

Fig. 7. Ethene yield as a function of temperature over nickel oxide-based catalysts issued from Protocol 3* (Ni removed from $NiO_{\_SG}$), obtained by ethane ODH. Reaction conditions: 10% C_2H_6/10% O_2/80% He (a) and 10% C_2H_6/5% O_2/85% He (b), W/F = 0.6 g s/mL.

selectivities (62–64%) and higher surface areas (110–145 m^2/g), as compared with $NiO_{\_SG}$ (Table 3).

5. Discussion

5.1. Activity

By compiling the catalytic results obtained on all NiO and Nb-containing nickel oxides (Tables 3 and 6), it appears that mass-specific ethene production rates are quasi-stable at Nb loading up to 4 at.% (with two higher values obtained with $Nb_{0.03}$–$Ni_{0.97}O$ and $Nb_{0.04}$–$Ni_{0.96}O$), before decreasing with increasing Nb content at higher loadings. On the other hand, intrinsic ethane ODH rates continuously decrease with increasing Nb content in the NiO samples. Activities of Nb_{1-x}–Ni_xO represent at 300 °C only 30–60% ($0.96 \leqslant x \leqslant 0.99$) and 5–25% ($0.80 \leqslant x \leqslant 0.95$) of the activity of $NiO_{\_SG}$ (Table 5). However, NiO contributes to 50–100% of the total surface area at low Nb loading and to 20%, at the very least, of the total surface area at high Nb loading (48/225). Hence, the extent of the continuous decrease in the intrinsic ethane ODH rates cannot be solely explained by the increasing presence of a potentially inactive Nb-rich mixed oxide phase (Fig. 3) added to similarly active NiO particles. This suggests that the presence of Nb somehow reduces the ethane ODH activity of NiO and that the interaction between the Nb-rich Ni–Nb mixed oxide phase and NiO crystals cannot be ignored.

Apparent activation energies for Nb–NiO-catalyzed ethane ODH are clearly not as affected by the Nb content as in [36]. Indeed, only a minor decrease in apparent activation energies from about 80 (±1) kJ/mol to 77 (±1) kJ/mol at high Nb contents is observed, instead of the reported 78 to 60 kJ/mol decrease. Hence, no major change in the nature of the active site is expected; it seems that the active site responsible for ethane ODH is hardly affected by the presence of Nb. The values for apparent activation energies are in agreement with those reported for ethane ODH catalyzed by unsupported nickel oxide (75 kJ/mol) [31] or by supported Ni/SiO_2 (86 kJ/mol) [31]. They are also consistent with those reported for Mo–V–Ni-catalyzed ethene production (18 kcal/mol = 75 kJ/mol) [45].

5.2. Selectivity

Apparent activation energies for total oxidation are systematically higher than those for selective ethene formation for Nb loadings >4 at.%, whatever the O_2 partial pressure (5 kPa or 10 kPa), which is in agreement with [44]. This means that, over Nb-rich NiO samples, high selectivities to ethene are favored by lower temperatures, as observed on Fig. 8a. On $NiO_{\_SG}$ and lightly-doped nickel oxides, the selectivity to ethene is quite stable over the 200–400 °C temperature range (Fig. 8a). This is consistent with the similar activation energies found for ethene production and CO_2 formation (Tables 3 and 6). This stability is slightly disturbed though (Fig. 8b) when the reaction is carried out in a gas mixture containing more oxygen (10 vol.% instead of 5 vol.%). This is due to the higher sensitivity of the CO_2 formation rate, as compared with the ethene production rate, to the partial pressure of oxygen (10 kPa). It is the case for all catalysts, which all exhibit a lower selectivity in the gas feed containing a higher O_2/ethane ratio (Fig. 8).

As the Nb content increases, apparent activation energy for ethene production decreases slightly, while the apparent activation energy for CO_2 formation increases (Tables 3 and 6). The resulting increasing difference between activation energies for ethene production and total oxidation, with no major change on the activation energy of the overall ethane ODH process, suggests that the presence of Nb does not modify the key catalytic steps of the NiO-catalyzed ethane ODH process but slightly modifies the electronic/geometric nature of the sites responsible for ethene production and CO_2 formation. It is also consistent with an increasing ratio of selective versus unselective surface species at low temperature in the initial stage of ethane ODH.

Selectivity to ethene indeed gradually increases with increasing Nb content at low conversion (Fig. 9) until a maximum is reached at the 15 at% loading, whatever the oxygen/ethane ratio. $Nb_{0.15}$–$Ni_{0.85}O$ achieves the maximum selectivity to ethene of 92% at 1% ethane conversion (Fig. 9a). The selectivity of the sample containing more than 4 at.% Nb, however, rapidly decreases with increasing conversion, but at 15% (Fig. 9a) or 20% (Fig. 9b) conversion, $Nb_{0.05}$–$Ni_{0.95}O$ remains more selective than Nb_{1-x}–Ni_xO with $x > 0.95$. The rate of decrease becomes faster with increasing Nb content; it is fastest over $Nb_{0.20}$–$Ni_{0.80}O$. This suggests that highly loaded Nb–NiO nanocomposites contain active sites for the consecutive total oxidation of ethene (ethane over-oxidation) at 330 °C [46]. On the other hand, the selectivity of NiO and the lightly-loaded samples is pretty stable over the range of conversions considered, especially at low O_2/ethane ratio (Fig. 9a), indicating that selectivity is essentially compromised, at 330 °C, by the parallel total oxidation of ethane to CO_2.

5.3. Reducibility

Ethane ODH is known to proceed via a Mars and Van Krevelen mechanism, which includes the following elementary steps [47]:

1. Interactions of ethane with the surface of the catalyst (weak/physical adsorption).
2. Rupture of the C–H bond leading to the formation of the ethyl species.
3. Reaction of the ethyl species with an adjacent surface oxygen (β-elimination) and formation of ethene.
4. Reoxidation of the catalyst surface by dissociative adsorption of molecular oxygen.

Hence TPR experiments were performed in order to evaluate the redox properties of the materials. The TPR profile of $NiO_{\_SG}$ (Fig. 10a) consists in a main reduction peak at 310 °C, associated with a shoulder at 250 °C. When Nb is incorporated into the sample, the main reduction peak shifts to 370 °C in $Nb_{0.01}$–$Ni_{0.99}O$; it further shifts toward higher temperatures as the Nb content increases, until it reaches 430 °C in $Nb_{0.20}$–$Ni_{0.80}O$. This peak can be attributed to the main $Ni^{2+} \rightarrow Ni^0$ transformation [48]. Its shift toward higher temperatures thus shows that NiO reducibility gradually diminishes, as the Nb content increases. This suggests that the first step of ethane ODH (reduction of the catalyst surface) could be hindered in Nb–NiO composites. As this step is generally considered to be limiting in ethane ODH, this could explain the lower activity of the Nb-containing nickel oxides.

Besides, the shoulder occurring 60 °C below the reduction temperature of the main peak is absent from the profiles of the composites containing more than 5 at.% Nb. The shoulder can be attributed in $NiO_{\_SG}$ to the reduction of the Ni^{3+} cations present in non-stoichiometric NiO to Ni^{2+}. It indicates an over-stoichiometry of oxygen in NiO crystal structure, hence the presence of cationic vacancies and non-stoichiometric O^- species [48]. O^- species being generally considered as highly active and poorly selective, the absence of the most active of them could account for both the lower activity and the higher selectivity of the highly loaded Nb–NiO composites.

Furthermore, the total hydrogen consumption, normalized to the theoretical amount of Ni atoms in the sample, slightly decreases with increasing Nb content (Fig. 10b), as also observed with Nb–Ni oxides prepared by evaporation [34]. This further supports the fact that fewer active/reducible oxygen species are

Table 6
Catalytic properties of nickel-based oxides in low-temperature ethane ODH (Reaction conditions: 10% C_2H_6/5% O_2/85% He, W/F = 0.6 g s/mL, temperature ramped at 1°/min from 200 to 400 °C).

Catalyst	Ethane conversion (%)		Selectivity (%)		Ethene yield (%)		Ethane ODH rate (mol/m^2/s)		Ethene production rate (mol/g/s)		Ea (kJ/mol) [a]		
	300 °C	350 °C	300 °C	350 °C	300 °C	350 °C	300 °C (×10^{-8})	350 °C (×10^{-8})	300 °C (×10^{-7})	350 °C (×10^{-6})	ODH	Ethene	CO_2
NiO$_{\text{\_oxalic acid}}$	12.7	29	64	64	8.2	19	1.46	3.4	6.1	1.4	78	80	76
NiO$_{\text{\_NH4OH}}$	11.0	19	16	32	1.7	6	1.37	2.4	1.3	0.5	99	108	93
NiO$_{\text{\_SG}}$	12.5	26	64	64	7.8	18	2.02	4.3	5.8	1.3	82	83	78
$Nb_{0.01}$–$Ni_{0.99}O$	9.3	26	67	66	6.3	17	1.23	3.4	4.7	1.3	80	79	80
$Nb_{0.02}$–$Ni_{0.98}O$	9.6	26	71	70	6.8	19	0.80	2.2	5.1	1.4	79	79	79
$Nb_{0.03}$–$Ni_{0.97}O$	13.8	31	70	71	9.7	22	0.94	2.1	7.2	1.6	77	77	78
$Nb_{0.04}$–$Ni_{0.96}O$	13.9	31	71	71	9.8	22	0.71	1.6	7.3	1.6	78	77	80
$Nb_{0.05}$–$Ni_{0.95}O$	6.6	22	82	77	5.4	17	0.38	1.3	4.0	1.3	81	81	88
$Nb_{0.10}$–$Ni_{0.90}O$	5.4	16	82	78	4.4	12	0.25	0.8	3.3	0.9	76	76	80
$Nb_{0.15}$–$Ni_{0.85}O$	4.8	14	86	80	4.2	11	0.16	0.5	3.1	0.8	76	77	83
$Nb_{0.20}$–$Ni_{0.80}O$	2.6	8	85	80	2.2	7	0.10	0.3	1.6	0.5	77	77	88

[a] Calculated by the Arrhenius law, on the variations of the mass-specific rates of ethane consumption and net ethene and CO_2 production (mol/g/s) as a function of the temperature (K^{-1}), in the 240–310 °C temperature range.

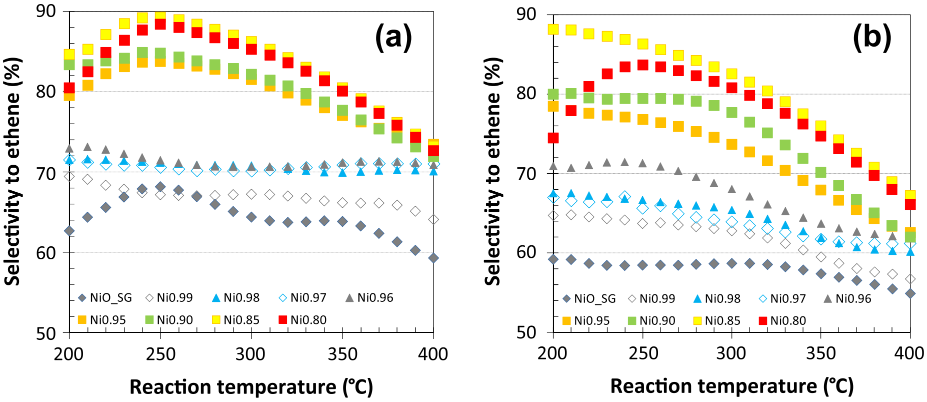

Fig. 8. Selectivity to ethene as a function of temperature, obtained in ethane ODH over NiO$_{\text{\_SG}}$ (◆), $Nb_{0.01}$–$Ni_{0.99}O$ (◇), $Nb_{0.02}$–$Ni_{0.98}O$ (▲), $Nb_{0.03}$–$Ni_{0.97}O$ (◇), $Nb_{0.04}$–$Ni_{0.96}O$ (▲), $Nb_{0.05}$–$Ni_{0.95}O$ (🟧), $Nb_{0.10}$–$Ni_{0.90}O$ (🟩), $Nb_{0.15}$–$Ni_{0.85}O$ (🟨), and $Nb_{0.20}$–$Ni_{0.80}O$ (🟥). Reaction conditions: 10% C_2H_6/5% O_2/85% He (a) and 10% C_2H_6/10% O_2/80% He (b), W/F = 0.6 g s/mL.

present in the Nb-rich NiO catalysts. It can stem from the presence of a physical barrier that allows access to fewer O^- species. This is consistent with the "geometric" effect proposed by Millet et al. [36], in which the presence of a Nb-rich mixed oxide phase on NiO nanocrystallites (Fig. 5) covers part of the active sites, thereby protecting them from reduction and inhibiting the rate-limiting step of ethane ODH. The lower hydrogen consumption can also indicate that NiO crystallites are more reduced in Nb-rich Nb–NiO composites. This could result from doping of the NiO crystal structure with Nb cations, as proposed by Lemonidou and Heracleous [34]. Filling cationic vacancies of the nickel oxide structure would indeed lead to reduction of 2, 4 or 5 Ni^{3+} to 2, 4 or 5 Ni^{2+}, depending on the valency of the Nb cation. This "electronic" effect of Nb on NiO would also lead to a modification of the active sites, which could become less active and more selective.

Hence, increasing the Nb content in the Nb–NiO composites decreases both the number of reducible species available and the reducibility of these species. When Nb–NiO nanocomposites are prepared by the citrate method, their activity in low-temperature ethane ODH can thus be correlated with their redox properties, the most reducible catalysts being the most active ones. This is in contrast with what was previously reported for supported NiO [28] and for Nb–Ni oxides prepared by evaporation [34]. In the latter case, the incorporation of Nb indeed caused the main reduction peak to shift toward *lower* temperatures. This can be explained by a size effect. Indeed, lattice oxygen diffuses much more efficiently in smaller oxides crystallites, due to the higher surface-to-volume ratio, and smaller crystallites are thus more easily reduced than larger ones. Hence, the lower reduction temperature of 13 nm NiO$_{\text{\_SG}}$ (310 °C, Fig. 10a), as compared with that reported for the 32 nm NiO reference used by Lemonidou and Heracleous (415 °C) [34]. Increasing the Nb content in the Nb–NiO composites prepared by evaporation affects the NiO crystallite size and the reduction temperature accordingly, the smallest NiO crystallites (15 nm) obtained for the $Ni_{0.8}Nb_{0.2}$ composition being the most easily reduced (340 °C) [34]. On the other hand, the reducibility of the smaller NiO crystallites obtained in high surface area Nb–NiO nanocomposites prepared by the citrate method (7–13 nm, Table 2), is not determined by the size effect.

5.4. Stability

The fresh non-stoichiometric nickel oxide-based nanocomposites prepared by the citrate method are all black in color after calcination at 450 °C. However, nickel oxides containing more than 5 at.% Nb turn greenish upon ethane ODH, indicating modification under reaction conditions and suggesting in particular the formation of more stoichiometric NiO. The stability of $Nb_{0.01}$–$Ni_{0.99}O$, $Nb_{0.05}$–$Ni_{0.95}O$, and $Nb_{0.15}$–$Ni_{0.85}O$ versus time-on-stream has thus been investigated (Fig. 11). It turns out that 11%, 18%, and 44% of the original activities are lost in 72 h for $Nb_{0.01}$–$Ni_{0.99}O$, $Nb_{0.05}$–$Ni_{0.95}O$ and $Nb_{0.15}$–$Ni_{0.85}O$, respectively, (Table 7), of which about one quarter (2.5%), one third (6.5%) and one half (25%) are lost within the first 4 h at 330 °C. Hence, both the extent and the

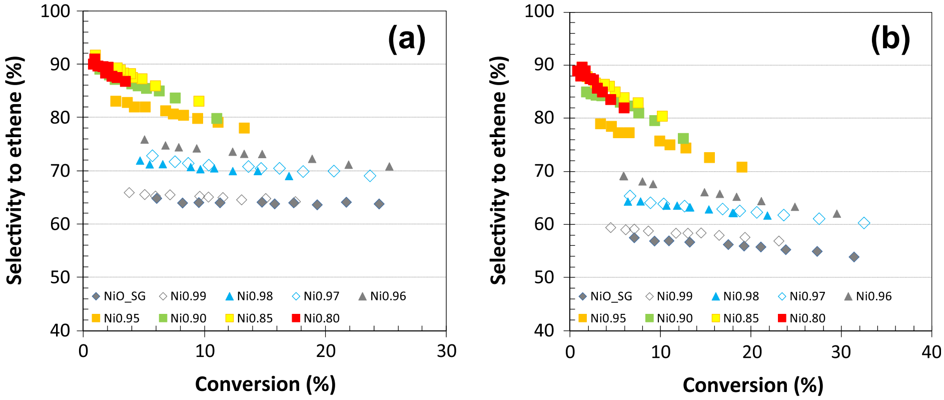

Fig. 9. Selectivity to ethene as a function of ethane conversion, obtained in ethane ODH over NiO_SG (◆), $Nb_{0.01}$–$Ni_{0.99}O$ (◇), $Nb_{0.02}$–$Ni_{0.98}O$ (▲), $Nb_{0.03}$–$Ni_{0.97}O$ (◇), $Nb_{0.04}$–$Ni_{0.96}O$ (▲), $Nb_{0.05}$–$Ni_{0.95}O$ (🟧), $Nb_{0.10}$–$Ni_{0.90}O$ (🟩), $Nb_{0.15}$–$Ni_{0.85}O$ (🟨), and $Nb_{0.20}$–$Ni_{0.80}O$ (🟥). Reaction conditions: 10% C_2H_6/5% O_2/85% He (a) and 10% C_2H_6/10% O_2/80% He (b), T = 330 °C.

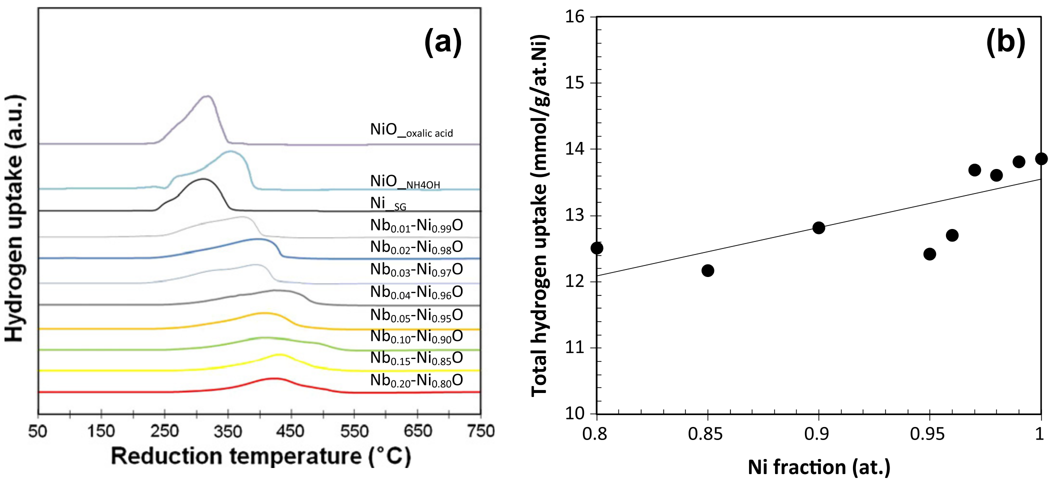

Fig. 10. Temperature programmed reduction spectra of all catalysts (a) and normalized total hydrogen uptake as a function of the theoretical Ni fraction in the Nb–NiO composites (b).

rate of deactivation in ethane ODH increases with increasing Nb content in the catalyst. This is accompanied by a slight increase in selectivity (Fig. 11b) for high Nb contents and no significant change of selectivity for $Nb_{0.01}$–$Ni_{0.99}O$ (66%).

Deactivation is thus not a function of initial activity; the least active catalysts, i.e., those containing a large amount of niobium, are actually also the least stable (Fig. 11a). For $Nb_{0.01}$–$Ni_{0.99}O$ and $Nb_{0.05}$–$Ni_{0.95}O$, the loss of activity correlates quite well with the loss of surface area observed (Table 7), suggesting that the intrinsic activity of these catalysts is retained. For $Nb_{0.15}$–$Ni_{0.85}O$, the loss of activity slightly exceeds the loss of surface area, indicating that its intrinsic activity decreases with time-on-stream. This is associated with a significant shift of the main reduction peak toward higher temperature in the used catalyst (Table 7), indicating that the less reducible, spent $Nb_{0.15}$–$Ni_{0.85}O$ is less efficient for activating ethane.

It is consistent with $Nb_{0.15}$–$Ni_{0.85}O$ being partially reduced during ethane ODH and NiO becoming near-stoichiometric (green). The consumption of non-stoichiometric surface oxygen species during the first, limiting step of the ODH reaction indeed causes both the creation of an oxygen vacancy and the reduction of the two neighboring Ni^{3+} cations to Ni^{2+} species in the NiO structure. It is possible that reoxidation of the Mars Van Krevelen catalyst, normally occurring via dissociative adsorption of molecular oxygen on the oxygen vacancy and reoxidation of the two neighboring Ni^{2+} species to Ni^{3+} cations, is hindered by the presence of large amount of Nb (15 at.%). It is not clear whether this could be related to the reorganization/restructuration of the Nb–NiO nanocomposite suggested by BET results (Table 7), which still leaves XRD patterns rather unchanged. Would instability/mobility of the niobium-rich mixed oxide amorphous nanolayer at immediate proximity of NiO surface or migration of species toward blocking access to oxygen vacancies be involved? It seems that inhibition of the catalyst reoxidation, i.e., refill of the oxygen vacancies created by the ODH reaction, anyhow causes loss of active sites. Deactivation could thus be attributed to irreversible consumption of active oxygen species which are not replenished.

Hence, although Nb generally enhances selectivity in NiO-catalyzed low-temperature ethane ODH [49], it is clear that its overall positive effect (taking into account both productivity and stability) depends on the level of loading, the chemical form of Nb and the interaction between Nb with NiO (solid solution, demixed oxide, etc.) in the catalyst. These three parameters are clearly interconnected and are a function of the method of preparation. Among the catalysts produced by the citrate method, NiO_SG displays the best performance ever displayed by nickel oxides; it is also the most stable catalyst in ethane ODH. The presence of 3–4 at.% Nb

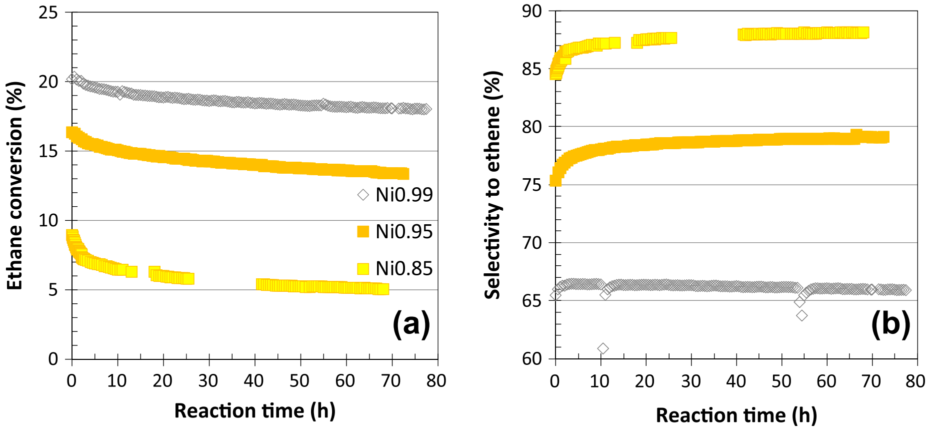

Fig. 11. Catalytic activity (a) and selectivity (b) of Nb$_{0.01}$–Ni$_{0.99}$O (◇), Nb$_{0.05}$–Ni$_{0.95}$O (🟧) and Nb$_{0.15}$–Ni$_{0.85}$O (🟨) in low-temperature ethane ODH as a function of time. Reaction conditions: 10% C_2H_6/5% O_2/85% He, *T* = 330 °C, W/F = 0.6 g s/mL.

Table 7
Comparison of BET and TPR data obtained on selected catalysts before and after stability test (10% C_2H_6/5% O_2/85% He, *T* = 330 °C, W/F = 0.6 g s/mL, *t* = 72 h).

Catalyst	BET surface area	% loss of activity (Fig. 11)			Temperature of main reduction peak (°C)		Total hydrogen uptake (mmol/g/at. Ni)	
	Fresh (m^2/g)	Used (m^2/g)	% loss		Fresh	Used	Fresh	Used
Nb$_{0.01}$–Ni$_{0.99}$O	56	49	13	11	375	362	13.8	13.2
Nb$_{0.05}$–Ni$_{0.95}$O	130	105	19	18	408	410	12.4	13.7
Nb$_{0.15}$–Ni$_{0.85}$O	225	142	37	44	430	460	12.2	13.5

increases both conversion and selectivity, i.e., overall catalyst efficiency, without significantly compromising stability. Although the specificities of these samples are not fully understood, it appears that the corresponding NiO crystallites are the smallest obtained in this study (7 nm) and the smallest studied so far. They are also the only ones presenting a slight increase in the cubic cell parameter (Table 2), as expected from the dependency of the cell parameter on the crystallite size [50].

6. Conclusion

In addition to leading to highly efficient and stable NiO catalysts for ethane ODH, the development of the citrate method for the synthesis of Nb–NiO composites shows that:

1. The method of preparation has a critical impact on the physico-chemical and catalytic properties of Ni and Nb–Ni oxides; Nb-containing NiO catalysts prepared in the presence of citric acid in a sol–gel method behave differently in low-temperature ethane ODH than the catalysts prepared by the evaporation method from nickel nitrate and ammonium niobium oxalate.
2. Nanocrystalline NiO is obtained (<13 nm) in all samples.
3. In the presence of niobium, an amorphous phase is formed; it is attributed to a Nb-rich mixed oxide phase close to $NiNb_2O_6$.
4. Large metallic Ni particles (38–102 nm), representing 14–18 wt.% of the nanocomposite, are produced in the presence of less than 1 at.% Nb.
5. The presence of >2 at.% Nb in Nb–Ni–citrate prevents the formation of the metallic Ni phase upon calcination of the gel at 450 °C; it also reduces the crystallite size of the formed NiO.
6. The presence of >2 at.% Nb significantly increases the overall surface area of the nanocomposite, up to 225 m^2/g for Nb$_{0.15}$–Ni$_{0.85}$O, which is a mixture of 10 nm NiO crystallites and ca. 1–2 nm amorphous Nb-rich mixed oxide.
7. When prepared by the citrate method, Nb$_{0.15}$–Ni$_{0.85}$O is not the optimum catalyst for ethane ODH, neither in terms of productivity nor in terms of stability. The positive effect of Nb in NiO-catalyzed low-temperature ethane ODH is obtained only at low levels of Nb contents (3–4 at.%), at which high activity and stable selectivity are obtained.
8. At Nb loading >5 at.%, amorphous interparticle Nb-rich oxide layers lead to lower activity and, at the same time, cause deactivation of the NiO catalyst, which increases with increasing Nb content.
9. The activity of these nanometric oxides in low-temperature ethane ODH seems to be directly related to their redox properties, the most reducible catalysts being the most active.

Since catalytic properties of Nb–NiO systems in low-temperature ethane ODH are so critically dependent on the method of preparation used, it is expected that further improvement can be made by optimizing catalyst preparation.

Acknowledgments

The authors acknowledge the KAUST Imaging and Characterization core lab, and scientific and technical assistance of Drs. Mohamed Nejib Hedhili (XPS), Rachid Sougrat and Lan Zhao (TEM). S.O.-C. wishes to thank Dr. G. Bergeret and F. Bosselet (IRCELYON, France) for fruitful discussions on Rietveld analysis, as well R. Jardin (Bruker).

References

[1] T.D. Foley, S.W. Sohn (UOP LLC), US Patent 6407301, 2002.
[2] M. Ghadrdan, R. Karimzadeh, R. Bozorgmehri, <http://www.nt.ntnu.no/users/skoge/prost/proceedings/ecce6_sep07/upload/1424.pdf>.
[3] <http://www.plastemart.com/plasticnews_desc.asp?news_id=19458>.
[4] C.N. Eng, S.C. Kang, S. Choi, S.H. Oh, Y.K. Park, Advanced Catalytic OlefinsTM, KBR Internal Reference Paper 2015, 2002. <http://www.kbr.com/Newsroom/Publications/technical-papers/A-Catalytic-Cracking-Process-for-Ethylene-and-Propylene-from-Paraffin-Streams.pdf>.
[5] V.R. Choudhary, S.A.R. Mulla, AIChE J. 43 (1997) 1545.
[6] E.M. Kennedy, N.W. Cant, Appl. Catal. 75 (1991) 321.
[7] S.A.R. Mulla, O.V. Buyevskaya, M. Baerns, J. Catal. 197 (2001) 43.
[8] S. Gaab, M. Machli, J. Find, R.K. Grasselli, J.A. Lercher, Top. Catal. 23 (2003) 151.
[9] O.V. Buyevskaya, D. Wolf, M. Baerns, Catal. Today 62 (2000) 91.
[10] S.J. Conway, J.H. Lunsford, J. Catal. 131 (1991) 513.

[11] H.M. Swana, A. Toebes, J.R.H. Ross, Catal. Today 13 (1992) 201.
[12] D.J. Wang, M.P. Rosynek, J.H. Lunsford, J. Catal. 151 (1995) 155.
[13] F. Dons, R. Pirone, G. Russo, J. Catal. 209 (2002) 51.
[14] H.X. Dai, C.F. Ng, C.T. Au, Catal. Lett. 57 (1999) 115.
[15] H.X. Dai, C.F. Ng, C.T. Au, Stud. Surf. Sci. Catal. 130 (2000) 1757.
[16] H.X. Dai, C.F. Ng, C.T. Au, J. Catal. 189 (2000) 52.
[17] H.X. Dai, C.F. Ng, C.T. Au, J. Catal. 193 (2000) 65.
[18] H.X. Dai, C.F. Ng, C.T. Au, J. Catal. 197 (2001) 251.
[19] M. Huff, P.M. Torniainen, L.D. Schmidt, Catal. Today 21 (1994) 113.
[20] Y. Liu, P. Cong, R.D. Doolen, S. Guan, V. Markov, L. Woo, S. Zey, U. Dingerdissen, Appl. Catal. A. 254 (2003) 59.
[21] K.-I. Nakamura, T. Miyake, T. Konishi, T. Suzuki, J. Mol. Catal. A 260 (2006) 144.
[22] X. Zhang, J. Liu, Y. Jing, Y. Xie, Appl. Catal. A 240 (2003) 143.
[23] X. Zhang, Y. Gong, G. Yu, Y. Xie, J. Mol. Catal. A 180 (2002) 293.
[24] F. Cavani, N. Ballarini, A. Cericola, Catal. Today 127 (2007) 113.
[25] E.M. Thorsteinson, T.P. Wilson, F.G. Young, P.H. Kasai, J. Catal. 52 (1978) 116.
[26] P. Botella, E. Garcia-Gonzalez, A. Dejoz, J.M. Lopez Nieto, M.I. Vazquez, J. Gonzalez-Calbet, J. Catal. 225 (2004) 428.
[27] Y. Liu, P. Cong, R.D. Doolen, S. Guan, V. Markov, L. Woo, S. Zeyß, U. Dingerdissen, Appl. Catal. A 254 (2003) 59.
[28] Y. Schuurman, V. Ducarme, T. Chen, W. Li, C. Mirodatos, G.A. Martin, Appl. Catal. A 163 (1997) 227.
[29] B. Halpern, J.E. Germain, J. Catal. 37 (1975) 44.
[30] E. Heracleous, A.F. Lee, K. Wilson, A.A. Lemonidou, J. Catal. 231 (2005) 159.
[31] V. Ducarme, G.A. Martin, Catal. Lett. 23 (1994) 97.
[32] E. Heracleous, A.A. Lemonidou, J. Catal. 270 (2010) 67.
[33] B. Solsona, J.M. López Nieto, P. Concepción, A. Dejoz, F. Ivars, M.I. Vázquez, J. Catal. 280 (2011) 28.
[34] E. Heracleous, A.A. Lemonidou, J. Catal. 237 (2006) 162.
[35] E. Heracleous, A.A. Lemonidou, J. Catal. 237 (2006) 175.
[36] B. Savova, S. Loridant, D. Filkova, J.M.M. Millet, Appl. Catal. A 390 (2010) 148.
[37] Y. Wu, Y. He, T. Wu, W. Weng, H. Wan, Mater. Lett. 61 (2007) 2679.
[38] Bruker Advanced X-ray Solutions TOPAS V4.2, Technical Reference, Bruker AXS, Karlsruhe, Germany, 2009.;
R.W. Cheary, A.A. Coelho, J. Appl. Cryst. 25 (1992) 109.
[39] E. Heracleous, A. Delimitis, L. Nalbandian, A.A. Lemonidou, Appl. Catal. A 325 (2007) 220.
[40] Q. Yang, J. Sha, X. Ma, D. Yang, Mater. Lett. 59 (2005) 1967.
[41] K. Sakitani, K.-I. Nakamura, N.-O. Ikenaga, T. Miyake, T. Suzuki, J. Jpn. Petrol. Inst. 53 (2010) 327.
[42] V. Mendez, V. Caps, S. Daniele, Chem. Commun. (2009) 3116.
[43] M.K. Bahl, J. Phys. Chem. Solids 36 (1975) 485.
[44] S.F. Ho, S. Contarini, J.W. Rabalais, J. Phys. Chem. 91 (1987) 4779.
[45] O. Desponds, R.L. Keiski, G.A. Somorjai, Catal. Lett. 19 (1993) 17.
[46] M.L. Rodríguez, D.E. Ardissone, E. Lopez, M.N. Pedernera, D.O. Borio, Ind. Eng. Chem. Res. 50 (2011) 2690.
[47] R. Grabowski, Catal. Rev. Sci. Eng. 48 (2006) 199.
[48] N.K. Kotsev, L.I. Ilieva, Catal. Lett. 18 (1993) 173.
[49] M.O. Guerrero-Pérez, A.E. Lewandowska, M.A. Bañares, Recent Patents Chem. Eng. 1 (2008) 201.
[50] S.A. Makhlouf, M.A. Kassem, M.A. Abdel-Rahim, J. Mater. Sci. 44 (2009) 3438.